

# Submicrometer Dimple Array Based Interference Color Field Displays and Sensors

H. J. Lezec,<sup>†,‡</sup> J. J. McMahon,<sup>§</sup> O. Nalamasu,<sup>||</sup> and P. M. Ajayan<sup>\*,||</sup>

*Thomas J. Watson Laboratory of Applied Physics, California Institute of Technology, Pasadena, California 91125, Centre National de la Recherche Scientifique, 3 rue Michel-Ange, 75794 Paris Cedex 16, France, and Center for Integrated Electronics and Department of Materials Science and Engineering, Rensselaer Polytechnic Institute, Troy, New York 12180*

Received October 15, 2006; Revised Manuscript Received December 10, 2006

## ABSTRACT

We report a technique for producing bright color fields over extended surfaces, via optical interference, with the capability of producing arbitrary visible colors in areas as small as  $100 \mu\text{m}^2$ . Periodic arrays of submicrometer dimples are fabricated on reflective silicon surfaces, and diffraction-induced mutual interference of light reflected from the upper and lower levels of the dimpled surfaces generates color depending on wavelength scaled dimple depth and periodicity. Colors of the entire visible spectrum can be generated by dimple arrays with different dimple depths. The topological permeability of such an open surface readily allows infusion of liquids, with different refractive indices, for color switching and detection. These easy to fabricate, scalable, robust devices, on solid as well as flexible supports, could find a wide range of applications such as cheap high-resolution printable dye/pigment-free displays, reliable index-of-refraction sensors with color readout for liquids, and lab-on-chip liquid flow monitors.

Though colors are generally created from pigments or chromophores, which absorb or emit light, they can also be produced from purely physical effects such as diffraction, scattering, and interference. Such effects are witnessed both in man-made systems such as holograms<sup>1</sup> and in nature such as in the vivid hues of a butterfly wing.<sup>2</sup> Over the past several years a number of interesting ideas have been reported to create regulated color fields in both sensing<sup>3</sup> and display applications.<sup>4–6</sup> Some of the most attractive approaches leverage interference based color generation, for example, using electrostatically actuated diffraction gratings for displays<sup>4</sup> or porous silicon or aluminum films on reflective surfaces for applications such as chemical or biological sensing.<sup>7–17</sup> In this approach we report here, the color generation is accomplished by periodic arrays of submicrometer dimples of carefully chosen depths and periodicity.

A transparent thin-film coating on a reflective substrate displays a modulated reflection spectrum with alternating high- and low-intensity features. This effect results from optical interference between light reflected at the two respective interfaces defined by the thin film. When such a

sample is illuminated with white light, a distinct color is perceived. This color is a sensitive function of the thickness  $d$  and the index of refraction  $n$  of the thin film. It is appealing to use color resulting from thin-film interference effects as a sensor to monitor changes in index of refraction of a given dielectric medium.<sup>3</sup> Conversely, it would also be interesting to induce intentional color changes, say for display applications, by varying the index of refraction of the medium facing the device. In the typical case of a solid thin film coating (such as  $\text{SiO}_2$  on Si), optical-interference-induced color is produced in the context of a fixed, static situation: neither  $n$  nor  $d$  can be readily changed in a dynamic manner in order to induce a color variation. If we make the transition from solid to a liquid dielectric media, it becomes a simple matter to exchange a liquid of one index for a liquid of another index, for example by sequential immersion, or by using a microfluidic system. However, it is not a straightforward matter to directly replicate the thin-film interference process obtained in the solid-film case. For example, it is difficult to stably form a liquid film with the uniform thickness and interface flatness required to yield a specific color.

Recently, porous silicon<sup>7–16</sup> and porous aluminum<sup>17</sup> have been investigated as materials for chemical or biological sensing. The reflection spectrum of thin films of such a material displays pronounced interference fringes as a

<sup>†</sup> Thomas J. Watson Laboratory of Applied Physics, California Institute of Technology.

<sup>‡</sup> Centre National de la Recherche Scientifique.

<sup>§</sup> Center for Integrated Electronics, Rensselaer Polytechnic Institute.

<sup>||</sup> Department of Materials Science and Engineering, Rensselaer Polytechnic Institute.

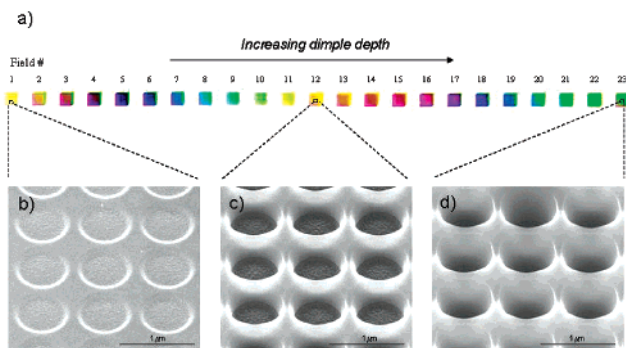


**Figure 1.** Visual effect of etching the surface of a reflective substrate (Si) with arrays of cylindrical cavities (dimples) of wavelength-scale periodicity, diameter, and depth. (a) Optical microscope image (in reflection, at normal incidence, using a 10 $\times$  objective lens), of a row of 23 dimple arrays ("fields") each of fixed periodicity ( $P = 800$  nm), size ( $11 \times 11$  dimples), and cavity diameter ( $f = 600$  nm). Dimple depth ( $d$ ) is increased from array to array, in 32-nm increments, from  $d = 96$  nm at the leftmost array position (field 1) to  $d = 800$  nm at the rightmost position (field 23). (b–d) SEM micrographs (45 $^\circ$  tilt) of detailed areas of dimple fields with  $d = 96$ , 448, and 800 nm, respectively (fields 1, 12, and 23, respectively).

function of wavelength. Detectable shifts in these interference fringes occur when the average index of refraction of the porous matrix is changed upon permeation with a chemical liquid or upon selective binding of biological molecules. Relatively thick (micrometer scale) porous films are normally used to provide sensitivity under the form of spectrally narrow (hence numerous) interference fringes. By use of a periodic electrochemical etch, one or more interference peaks can be enhanced and all others suppressed by varying the pore size as a function of depth position.<sup>10–16</sup> This spectral tailoring is achieved via a continuous periodic modulation of pore size<sup>10–13</sup> or a microcavity resonator structure consisting of a homogeneous porous layer trapped between a multilayer stack of films of alternating pore sizes (mirrors).<sup>14–16</sup> In all cases, due to a pore size substantially smaller than the wavelength of light, the material can be treated as laterally homogeneous, with optically smooth interfaces (e.g., porous Si/air and porous Si/substrate).

Here we investigate a new and powerful approach to making optical sensor and display devices in which we replace collinear interference of light reflected from two or more continuous optical interfaces by quasi-collinear interference of light diffracted from a single continuous interface with stepped height and wavelength scale features. This mesoscopic surface takes the form of a two-dimensional array of flat-bottomed cylindrical cavities (or dimples) etched into a flat substrate material that is opaque in the visible and highly reflective. A polished Si wafer constitutes a convenient choice for such a substrate, but any other reflective material would work. A typical device is shown in Figure 1, consisting of an  $11 \times 11$  square array of dimples milled, using a focused ion ( $\text{Ga}^+$ , 30 keV, 300 pA) beam (FIB) instrument, into the surface of a polished Si wafer.

For notational convenience, we designate the bottom surfaces of the dimples as B and the top surface of the substrate surrounding the dimple openings as A. Array

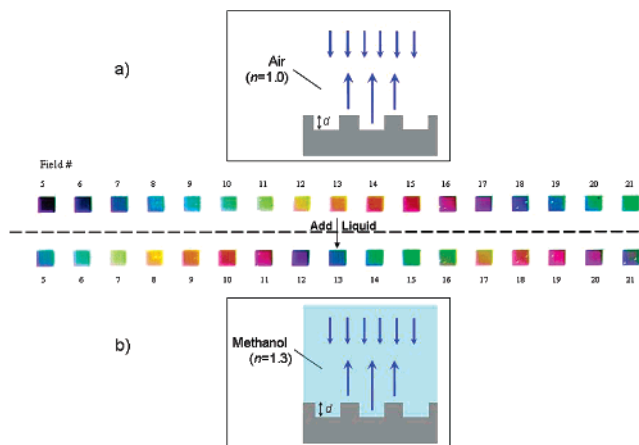


**Figure 2.** Observation of change of color in the dimple fields by varying the index of refraction ( $n$ ) of the dielectric medium facing the silicon surface. Optical image (in reflection, at normal incidence, using a 20 $\times$  objective lens) of selected area of row of Figure 1, extending from field 5 ( $d = 224$  nm) to field 21 ( $d = 736$  nm). (a) Array facing air ( $n = 1$ ). (b) Array facing methanol ( $n = 1.3$ ). Insets: schematic cross section of device, facing air and liquid, respectively.

geometry is configured according to a few simple design rules. Dimple diameter  $\phi$  is chosen to ensure that the cylindrical cavity forms a waveguide below cutoff, i.e., allows propagation of light down and back up the cavity. This can be achieved by choosing  $\phi > \lambda_v/2$ , where  $\lambda_v$  corresponds to the maximum wavelength of interest for device operation. Array period  $P$  is chosen to ensure that the unit-cell area corresponding to the bottom surface B,  $A_B = \pi\phi^2/4$ , is approximately equal to the unit-cell area corresponding to the top surface A,  $A_A = P^2 - \pi\phi^2/4$ . The material comprising surfaces A and B is identical. Thus, owing to the near-equal reflected intensity from top and bottom surfaces, respectively, maximum interference contrast can be obtained under plane wave illumination at normal incidence. Dimple diameter  $\phi$  is chosen to be wavelength or subscale, i.e., be comparable to the central wavelength of the range of operation of interest, i.e.,  $\phi \sim \lambda_c$ . This ensures significant diffraction at the exit of each cavity leading to strong lateral overlap and interference between light reflected from surfaces A and B. We tailor the device for operation in the visible and near-IR range ( $\lambda_v = 1000$  nm,  $\lambda_c = 650$  nm.) by choosing  $\phi = 600$  nm and  $P = 800$  nm. A beam diameter on the order of 30 nm ensures precise and reproducible definition of dimples with near-vertical side-walls and a well-defined flat bottom surface. A unique feature of FIB milling is the ability to tailor the dimple depth (from dimple to dimple or array to array) in a single fabrication step.

First we explore the effect of dimple depth  $d$  on the optical properties of such dimple arrays (Figure 1). A row of dimple fields is fabricated with  $d$  increasing linearly from field to field in constant increments of  $\Delta d = 32$  nm (keeping  $d$  constant within any given field). The row contains 23 fields (labeled 1 to 23), with  $d$  varying from 96 nm on one end of the row (field 1) to 800 nm on the other end of the row (field 23). Scanning electron microscopy (SEM) micrographs

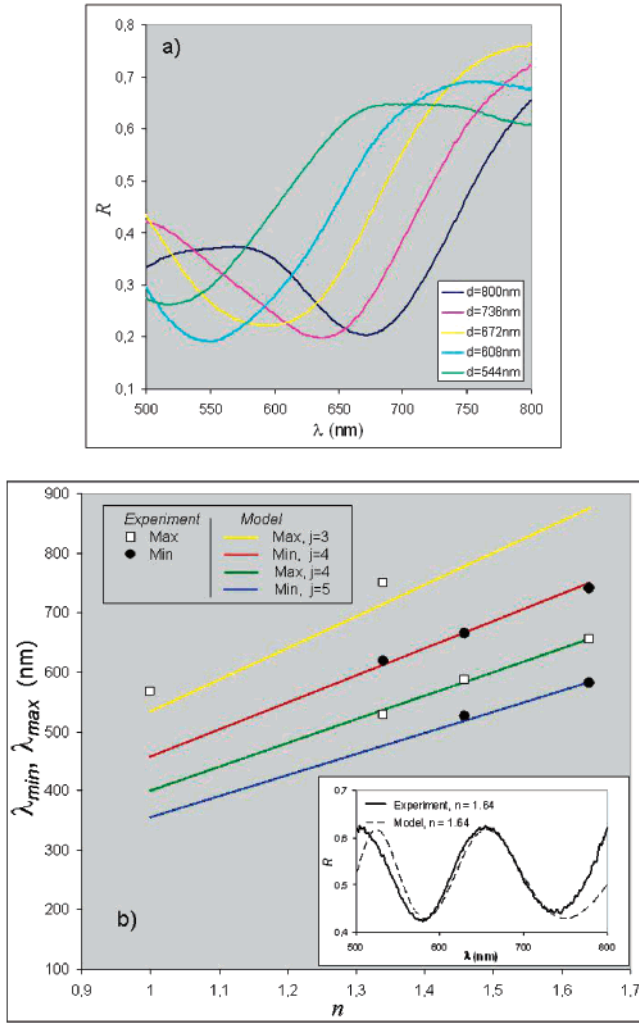


**Figure 3.** Experimental reflectance spectra, and correlation with model: (a)  $R(\lambda)$ , for arrays with dimple depths  $d = 544, 608, 672, 736,$  and  $800$  nm, respectively (fields 15, 17, 19, 21, and 23, respectively), with sample facing air ( $n = 1$ ). (b) Experimental reflectance data for array with  $d = 800$  nm (field 23), facing fluids of different dielectric constant  $n$ : symbols, experimental data; solid lines, predictions of simple interference model (from eqs 3a and 3b). Wavelength positions of minima and maxima in  $R$  and  $\lambda_{\min}$  and  $\lambda_{\max}$  are plotted as a function of  $n$ . Adjustable parameter  $j$  represents the interference orders explicit in eqs 3a and 3b which lead to best fit to experimental data for  $\lambda_{\min}$  and  $\lambda_{\max}$ . Inset: measured spectrum and corresponding interference model prediction (from eq 2) for the case  $n = 1.64$ .

of three representative fields (field 1 ( $d = 96$  nm), field 12 ( $d = 448$  nm), and field 23 ( $d = 800$  nm)) which span the explored dimple-depth range are shown in panels b, c, and d of Figure 1, respectively. The sample is then observed in reflection under white light illumination at normal incidence under an optical microscope, at a magnification of 10. Figure 1a illustrates a sequence of vivid color fields generated, as a result of the different dimple depths.

Next, we explore the effect of varying the index of refraction of the dielectric medium facing the sample. Figure 2a depicts a selected area of the device row of Figure 1a, ranging from field 5 ( $d = 224$  nm) to field 21 ( $d = 736$  nm), viewed at a magnification of 20 (reflection mode, white light, normal incidence). Note that the white dots apparent

in some of the color fields correspond to missing dimples resulting from fabrication error. Once again, the device is facing air. In Figure 2b, a thick (millimeter range) liquid film of methanol ( $n = 1.3$ ) is applied to the device. Each field is observed to undergo a dramatic color change. Insets in Figure 2a and Figure 2b illustrate our hypothesis for the interference process leading to the observation of color and color change. Colors are produced when light reflected from the bottom of the dimples (surface A) interferes with light reflected from the area surrounding the dimple exit surfaces (surface B). Angular diffraction of light when exiting the cavity as well as scattering from the top surface between the cavities leads to mixing and interference in the far field, including in the reconstructed microscope image. The variation of the net reflected beam as a function of wavelength (known as Fabry–Perot fringes) is what leads to the perception of a colored field. Adding a liquid above the sample surface readily fills the cavities and establishes a new difference in optical path length  $\delta$  between light reflected from bottom of dimple and top of dimple, from  $\delta = 2d$  to  $d = 2nd$ .

Taking an effective medium approach, we define  $r_A$  and  $r_B$  as the area-averaged complex amplitude reflection coefficient from surfaces A and B, respectively. The net far-field intensity resulting from lateral mixing of light reflected from A and B is given by

$$I_R(\lambda) = I_0 |r_A + r_B \exp(i \frac{2\pi}{\lambda_0} 2nd)|^2 \quad (1)$$

where  $\lambda_0$  and  $I_0$  are the vacuum wavelength and intensity of the incident light, respectively. Since surfaces A and B are composed of the same material,  $r_A$  and  $r_B$  have the same phase and we can write eq 1 as

$$I_R(\lambda) = I_0 \left( |r_A| + |r_B| \cos\left(\frac{2\pi}{\lambda_0} 2nd\right) \right)^2 \quad (2)$$

Minima and maxima occur for  $I_R$  at respective vacuum wavelength positions of

$$\lambda_{\min} = \frac{4nd}{2j - 1} \quad (3a)$$

and

$$\lambda_{\max} = \frac{2nd}{j} \quad (3b)$$

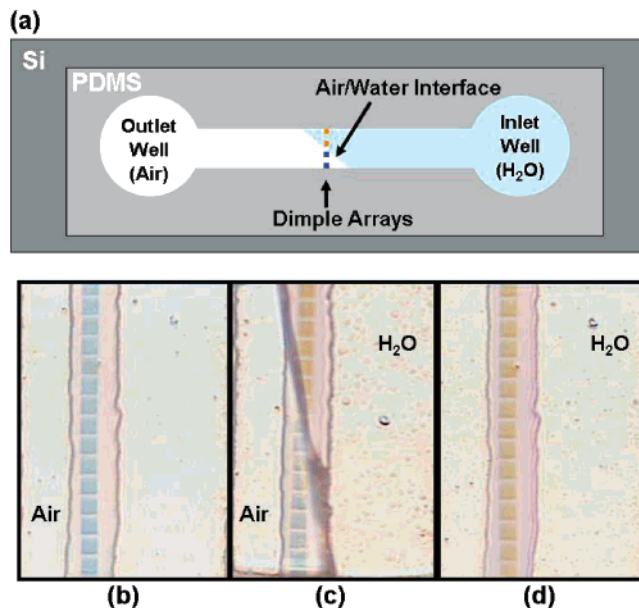
where  $j$  denotes the order of the interference.

Figure 3a shows experimental reflectance spectra,  $R(\lambda) = I_R(\lambda)/I_0$ , for arrays with dimple depths  $d = 544, 608, 672, 736,$  and  $800$  nm, respectively (fields 15, 17, 19, 21, and 23, respectively), with sample facing air ( $n = 1$ ). A broad, periodic modulation is evident across the spectral range. Varying the index of refraction  $n$  of the dielectric space facing the dimple array leads to a notable shift in the

reflectance spectrum. This effect is demonstrated in Figure 3b for the array with  $d = 800$  nm (field 23). In this figure, experimental values of  $\lambda_{\min}$  and  $\lambda_{\max}$  (in the range 400–900 nm) are plotted as a function of  $n$ , where  $n$  is varied by successively immersing the array in air, methanol, and two different index-matching fluids (Cargille series A and AA), respectively.

Predicted positions for  $\lambda_{\min}$  and  $\lambda_{\max}$  based on eqs 3a and 3b are also shown, using a self-consistent set of values for  $j$  which give the best match to the discrete experimental values. Interference orders  $j = 3, 4,$  and  $5$  are inferred to be effective over the considered spectral range for producing minima and maxima in the reflected signal. A maximum for a given interference order  $j$  occurs when the round-trip distance down and up the dimple,  $2nd$ , is equal to an integer number  $j$  of dielectric-adjusted wavelengths  $\lambda_0/n$ . This brings the wave reflected from the bottom of the dimple in phase with the wave reflected from the surface between the dimples, leading to a condition of constructive interference and maximum net reflected intensity. A minimum for the same order  $j$  entails fitting an extra half-wavelength  $\lambda_0/2n$  within that round-trip distance, leading to destructive interference and a minimum in the net reflected signal. The inset of Figure 3b displays the corresponding experimental reflectance spectrum  $R(\lambda)$  for the case  $n = 1.64$ . The theoretical spectral dependence of  $R$  based on the analytic expression of eq 2 is also plotted, using reflection amplitudes  $|r_A|$  and  $|r_B|$  as fitting parameters. A good match between the two curves is obtained, demonstrating the basic validity of the simple interference model proposed here.

The color change observed in Figure 2 suggests that the microfabricated wavelength-scaled dimple arrays might be useful as the core component of simple, environmentally friendly fluid-based sensors or display devices with direct color readout. To demonstrate the potential of dimple arrays for such an application, we fabricated dimple arrays on the bottom of a microfluidic channel and used this channel to deliver liquids of various indices of refraction to the surface of the arrays in a controlled manner (Figure 4). A column of dimple arrays (each of area  $10 \mu\text{m} \times 10 \mu\text{m}$ ) with geometrical parameters identical to those of Field 8 of Figures 1 and 2 ( $P = 800$  nm,  $\phi = 600$  nm, and  $d = 320$  nm) was first fabricated by FIB milling on the surface of an undoped, polished Si wafer. A transparent molded poly-(dimethylsiloxane) (PDMS) microchannel (channel with height  $10 \mu\text{m}$ , width  $200 \mu\text{m}$ , length 30 mm) connecting two wells on either end, was then placed over dimple arrays (Figure 4d). One well was filled with water, the other with air, and the sample was observed in reflection. An air–water interface was then positioned in the channel and repeatedly moved across the dimple arrays by pneumatic action. A sequence of optical micrographs documenting one such sweep is shown in parts a, b, and c of Figure 4, respectively. As the fluid moves across the dimples (from left to right in the channel), the color of the dimple fields is observed to switch from blue to orange. From a visual perspective, the color switch takes place concurrently and instantaneously with the progression of the liquid front over the dimple fields,



**Figure 4.** Microfluidic sensor and display with color readout, using printed submicrometer dimple arrays: (a) schematic plan view; (b–d) optical micrograph sequence showing effect of progression of air–water interface (from right to left in channel) across column of dimple arrays.

implying rapid filling of cavities with liquid. Videos 1 to 3 show real time recordings of color switching and are available as Supporting Information.

This demonstration suggests that our dimple arrays could be used to implement display devices ranging from ultra-miniature scale (for microfluidic applications such as high-contrast monitoring of liquid flow in lab-on-a-chip applications) to full-scale display screens. Recently, a color-display device<sup>18</sup> based on electrowetting<sup>19</sup> of dyed liquids in micro-fabricated pixels was demonstrated. The results presented here suggest that a similar device could be implemented in which the dye-provided colors could be replaced with colors generated by the robust dimple arrays on the surface of each pixel. The observed fluid-driven color switching could be used in cheap portable sensors for detection and identification. It could provide a convenient alternative to optical sensors based on infusion of liquids into porous silicon<sup>7–16</sup> films or colloidal crystal hydrogel films,<sup>20,21</sup> perhaps offering a significant speed advantage. Colors displayed here are provided without the use of polarizers, liquid crystals, and color filters, proving both simplicity and good luminosity. No sets of dyes or pigments are required to achieve color, suggesting excellent manufacturability and environmental friendliness. Finally, since colors result only from local surface topography, vast surfaces incorporating pixels of different base colors (such as RGB) could be printed in one single embossing step, on both rigid and flexible substrates. This could be implemented using straightforward techniques ranging from nanoimprint lithography for ultraminiaturized applications to stamping techniques for large-scale production.

**Acknowledgment.** This work was partially supported by the state of New York through NYSTAR, by the Caltech

**Supporting Information Available:** Experimental details and videos showing real time color switching. This material is available free of charge via the Internet at <http://pubs.acs.org>.

## References

- (1) Saxby, G., *Practical Holography*, 2nd ed.; Prentice Hall: Englewood Cliffs, NJ, 1994.
- (2) Srinivasarao, M. Nano-optics in the Biological world: Beetles, Butterflies, and Moths. *Chem. Rev.* **1999**, *99*, 1935.
- (3) Bailey, R. C. Parpia, M., and Hupp, J. T. Sensing via optical interference. *Mater. Today* 2005, April, 46.
- (4) Bloom, D. M. The Grating Light Valve: revolutionizing display technology. *SPIE Proc.* **1997**, *3013*, 165.
- (5) Hayes, R. A.; Feenstra, B. J. Video-speed electronic paper based on electrowetting. *Nature* **2003**, *425*, 383.
- (6) Hornbeck, L. J. Current Status of the Digital Micromirror Device (DMD) for Projection Television Applications. *IEDM Proc.* **1993**, 381.
- (7) Lin, V. S.; Motesarei, K.; Dancil, K.-P. S.; Sailor, M. J.; Ghadiri, M. R. A Porous Silicon-Based Optical Interferometric Biosensor. *Science* **1997**, *278*, 840.
- (8) Dancil, K.-P. S.; Greiner, D. P.; Sailor, M. J. A Porous Silicon Optical Biosensor: Detection of Reversible Binding of IgG to a Protein A-Modified Surface. *J. Am. Chem. Soc.* **1999**, *121*, 7925.
- (9) Gao, J.; Gao, T.; Sailor, M. Porous-silicon vapor sensor based on laser interferometry. *Appl. Phys. Lett.* **2000**, *77*, 901.
- (10) Cunin, F.; et al., Biomolecular screening with encoded porous-silicon photonic crystals. *Nat. Mater.* **2002**, *1*, 39.
- (11) Meade, S.; Yoon, M.; Ahn, K.; Sailor, M. Porous Silicon Photonic Crystals as Encoded Microcarriers. *Adv. Mater.* **2004**, *16*, 1811.
- (12) Link, J.; Sailor, M. Smart dust: Self-assembling, self-orienting photonic crystals of porous Si. *Proc. Natl. Acad. Sci. U.S.A.* **2003**, *100*, 10607.
- (13) Lorenzo, E., et al. Porous silicon-based rugate filters. *Appl. Opt.* **2005**, *44*, 5415.
- (14) Chan, S.; Horner, S.; Fauchet, P.; Miller, B. Identification of Gram Negative Bacteria Using Nanoscale Silicon Microcavities. *J. Am. Chem. Soc.* **2001**, *123*, 11797.
- (15) Anderson M.; et al. Sensitivity of the optical properties of porous silicon layers to the refractive index of liquid in the pores. *Phys. Status Solidi (A)* **2003**, *197*, 528.
- (16) Ouyang, H.; Christophersen, M.; Viard, R.; Milller, B.; Fauchet, P. Macroporous Silicon Microcavities for Macromolecule Detection. *Adv. Funct. Mater.* **2005**, *15*, 1851.
- (17) Pan, S.; Rothberg, L. Interferometric Sensing of Biomolecular Binding Using Nanoporous Aluminum Oxide Templates. *Nano Lett.* **2003**, *3*, 811.
- (18) Heikenfeld, J.; Steckl, A. J. High-transmission electrowetting light valves. *Appl. Phys. Lett.* **2005**, *86*, 151121-1.
- (19) Kwong, V. H.; Mossman, M. A.; Whitehead, L. A. Control of reflectance of liquid droplets by means of electrowetting. *Appl. Opt.* **2004**, *43*, 808.
- (20) Holtz, J.; Asher, S. Polymerized colloidal crystal hydrogel films as intelligent chemical sensing materials. *Nature* **1997**, *389*, 829.
- (21) Marshall, A.; Blyth, J.; Davidson, C.; Lowe, C. pH-Sensitive Holographic Sensors. *Anal. Chem.* **2003**, *75*, 4423.

NL062425A